THE JOURNAL OF PHYSICAL CHEMISTRY C

pubs.acs.org/JPCC Article

Surface Reactions of Low-Energy Argon Ions with Organometallic Precursors

Elif Bilgilisoy, Rachel M. Thorman, Jo-Chi Yu, Timothy B. Dunn, Hubertus Marbach, Lisa McElwee-White, and D. Howard Fairbrother*

Cite This: J. Phys. Chem. C 2020, 124, 24795−24808 Read Online

ACCESS | Metrics & More | Article Recommendations | Supporting Information

ABSTRACT: A combination of *in situ* X-ray photoelectron spectroscopy and mass spectrometry has been used to elucidate the elementary surface reactions initiated by the interaction of low-energy (860 eV) argon ions with three organometallic precursors [$Ru(CO)_4I_2$, $Co(CO)_3NO$, and $WN(NMe_2)_3$]. The effects of ion exposure on each precursor can be described by a largely sequential series of surface reactions. The initial step involves ion-induced decomposition of the precursor to create a nonvolatile deposit, followed by physical sputtering of the atoms in the deposit. For the precursors that contain CO ligands [$Ru(CO)_4I_2$ and $Co(CO)_3NO$], ion-induced decomposition is accompanied by desorption of the majority of the CO groups. This is in marked contrast to previous studies of low-energy electron-induced reactions with the same precursors where precursor decomposition yielded only partial desorption of the CO ligands. Conversely, argon ion bombardment of $WN(NMe_2)_3$ led to decomposition without ligand loss. For all three precursors, the initial ion-induced decomposition step was not accompanied by significant desorption of intact precursor molecules, while during subsequent physical sputtering of the deposited atoms, ligand-derived organic and inorganic contaminants were removed at higher rates than the metals. This indicates that controlled ion beam deposition conditions could be used to produce deposits with high metal contents from all three precursors. Comparison of low-energy electron-induced reactions of these three precursors with results of this investigation indicates that secondary electrons do not play an important role in the deposition process, but rather precursor decomposition occurs via efficient ion−molecule energy transfer. These reactions are discussed in the context of focused ion beam-induced deposition.

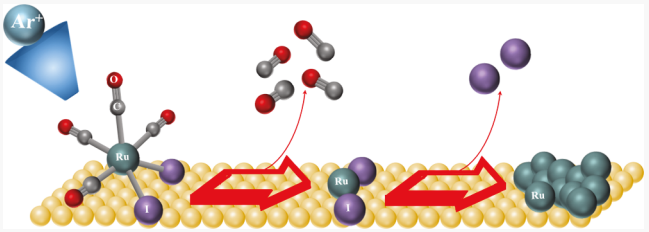

INTRODUCTION

Focused ion beam (FIB)-induced processing, which includes both FIB-induced deposition (FIBID) and FIB milling/sputtering, can be used to directly write nanoscale structures on both planar and nonplanar substrates without the application of masks or resists and selectively etch undesired material.[1,2] In FIBID, which is generally performed in a high vacuum chamber, a FIB is used to decompose transiently physisorbed organometallic precursor molecules, whereupon the nonvolatile metal-containing fragments will deposit onto the substrate while the volatile ligand fragments desorb.[2−4] FIBID, which has also been called FIB chemical vapor deposition (FIB-CVD), differs from other ion beam deposition techniques in that it uses FIBs to induce localized metal deposition from gaseous precursor molecules, as opposed to techniques such as ion beam-assisted deposition, which combines ion implantation and physical deposition methods.[5] In addition to depositing nanostructures,[6−9] both FIB sputtering and FIBID have also been adopted commercially as nanomodification techniques to make local repairs on commercial lithography masks[10] and edits on integrated circuits.[11] FIBID has also been used to fabricate probes (tips) for scanning probe microscopes[12] and to repair metallic connections on nanoscale devices.[13,14]

Although FIBID has a number of advantages as a nanofabrication technique, it also has several drawbacks. For example, use of the popular gallium liquid metal ion source can lead to gallium (Ga^+) implantation in structures. In the field of photomask repair, this can cause detrimental effects such as reducing the mask's optical transmission.[15] Other side effects of Ga^+ implantation include amorphization, surface damage, and low lateral resolution in deposited features.[4,16,17] As an alternative to the gallium liquid metal ion source, gas field ion sources using helium (He^+) and neon (Ne^+) have also been developed and integrated in FIB systems.[18] The use of He^+ has been shown to be particularly favorable in reducing the surface damage and lateral dimension of deposited structures

Received: August 11, 2020
Revised: October 13, 2020
Published: October 30, 2020

https://dx.doi.org/10.1021/acs.jpcc.0c07269
J. Phys. Chem. C 2020, 124, 24795−24808

compared to Ga^+ ions.[19] In one example, He^+-FIBID using the precursor $Co_2(CO)_8$ produced 10 nm laterally resolved lines on a silicon substrate, a 10-fold improvement in resolution compared to results obtained from the same precursor using Ga^+ ions.[20] Another unavoidable drawback of FIB systems is the competition between deposition and sputtering processes.[4] In FIB and FIBID, deposition reflects the efficiency with which the transiently adsorbed precursor molecules are converted/decomposed into nonvolatile fragments as a consequence of ion bombardment, while sputtering refers to the efficiency with which the nonvolatile fragments produced by precursor decomposition are subsequently removed by ion bombardment. Because Ga^+ ions typically have high sputter rates, the use of high beam currents during deposition can result in slow deposition rates and wasted precursor. To reduce these sputtering effects, lower beam currents and higher precursor fluxes (i.e., the ion-limited regime of FIBID) can be useful.[18] Despite the competition between deposition and sputtering in FIBID, the growth rate for deposits made from $Co_2(CO)_8$ with Ga^+-FIBID is 50 times higher than that with focused electron beam-induced deposition (FEBID), a related technique which utilizes a focused electron beam to create metal-containing structures from organometallic precursors, where deposition occurs in the absence of sputtering.[4]

Another notable issue with FIBID is that the deposit is often contaminated by material originating from the organometallic precursors (e.g., C, N, and O). For example, tungsten micro- and nanostructures made by FIBID have commonly been made from the precursor $W(CO)_6$; deposits made using 25−30 keV Ga^+ FIBs were found to be 34−40 at. % W,[2,21−23] while structures made using 30 keV He^+ FIBs were 47 at. % W.[24] Cobalt-containing FIBID-deposited micro- and nanostructures have primarily used the precursors $Co(CO)_3NO$ and $Co_2(CO)_8$. One study using $Co(CO)_3NO$ and 30 keV Ga^+ ions on SiO_2 produced deposits composed of 54 at. % Co, with contamination from gallium as well as the ligand elements.[25] Another study using $Co_2(CO)_8$ and 30 keV Ga^+ ions produced deposits with metal purities of 55−60 at. % Co.[4] Other precursors have been used to deposit a variety of metals, including $MeCpPtMe_3$, $Me_2Au(hfac)$, and (hfac)Cu-VTMS; however, no deposits made from these precursors have achieved >60 at. % metal purity without the use of additional purification methods.[26−29] From these considerations, it is clear that organometallic nanostructures created with FIBID commonly contain unwanted contamination, likely because of incomplete ligand desorption and/or ligand decomposition. Such contamination can lead to high electrical resistivity in deposits that are intended to be metallic contacts or high losses in deposits intended to be used as plasmonic structures, lessening their utility.

One approach to improving the application of FIBID in producing higher purity structures without the use of postdeposition processes is to gain insight into the molecular-level processes that underlie deposition and to understand how these processes vary for different precursors, including the balance between deposition and sputtering. Presently, however, there is a lack of understanding regarding the molecular-level events that lead to deposition in FIBID, in which one must consider not only the interactions between the high energy ion beam and both the substrate (target) surface and the precursor but also the possible interactions between the precursor and the secondary electrons produced by the impact of the high energy ion beam with the substrate. Interactions between the high-energy primary ions and the surface atoms (adsorbed precursor or substrate) are generally believed to involve collision-induced momentum/energy transfer from the incident ion to the surface atoms. If the incident ion strikes the substrate, a number of energetic surface atoms (ESAs) will be produced as a consequence of energy transfer from the incident ions to the surface atoms. These ESAs can transfer energy to transiently adsorbed precursor molecules, leading to deposition; this is known as the collision cascade model.[30] It has also been argued that the interactions of incident ions with the substrate may cause a localized temperature spike in the near-surface regime (the thermal spike model),[30] leading to localized thermal decomposition of precursor molecules. Under conditions where the coverage of precursor molecules is high (the "ion-limited" deposition regime), the contribution from direct interactions between the primary ion and the adsorbate molecule will also be important. Direct ion−molecule interactions will also dominate in processes such as cryo-FIBID, which has been shown to be an effective technique for creating nanostructures at high speed with excellent spatial fidelity.[31] A recent paper on Ga^+-FIBID using $W(CO)_6$ with the substrate at cryogenic temperatures demonstrated that cryo-FIBID is 600 times faster than conventional FIBID,[32] which suggests that cryo-FIBID (and thus, direct ion−molecule interactions) may become increasingly important as the field continues to develop. These ion−molecule interactions may result in ion-induced desorption of the precursor and/or reactions between the adsorbed precursor and the incident ions. Moreover, it is also possible that secondary electrons produced by the impact of the primary ion beam with the substrate (and adsorbate molecules) will also contribute to the deposition process (secondary electron model).

Given the multitude of events that can contribute to FIBID, a reductionist approach is appealing, wherein the number of potential processes is restricted. For example, gas-phase studies can isolate the interactions exclusively to the effects of individual ion−molecule collisions. A recent gas-phase study by Indrajith et al. demonstrated that ion−precursor interactions may be highly dependent on the velocity and mass of projectile ions. The study focused on the gas-phase fragmentation of $Fe(CO)_5$ by seven different ions (He^+, Ne^+, Ne^{4+}, Ar^+, Ar^{3+}, Kr^{3+}, and Kr^{17+}) with varying incident energies (3−225 keV), demonstrating that the interactions of the molecule with lighter ions (i.e., He^+) result in electronic excitation of the precursor molecule, while interactions with heavier ions (e.g., Ne^+ and Ar^+) are predominantly controlled by nuclear stopping power with weak contributions from electronic excitation and localized heating of the molecule.[31] An ultrahigh vacuum (UHV) surface science approach where organometallic precursors are physisorbed onto an inert substrate and bombarded with ions represents a step closer to the actual conditions under which FIBID is conducted. This approach has previously been used to elucidate the reactions between precursor molecules and low-energy electrons (500 eV) that lead to deposition in FEBID[33−36] and more recently to compare the electron and ion-induced decomposition reactions that lead to deposition in FEBID and FIBID.[37] Previous work demonstrated a clear difference in the extent of ligand desorption upon exposure of adsorbed (η^5-Cp)Fe-$(CO)_2Re(CO)_5$ to low-energy Ar^+ ions (860 eV) and electrons (500 eV). Upon electron irradiation, the sequence of bond-breaking reactions was found to consist of two steps: an initial

https://dx.doi.org/10.1021/acs.jpcc.0c07269
J. Phys. Chem. C 2020, 124, 24795−24808

step characterized by desorption of approximately half of the CO ligands, followed by a second step characterized by decomposition of the residual ligands. In contrast, argon ion bombardment of adsorbed $(\eta^5\text{-Cp})Fe(CO)_2Re(CO)_5$ led to complete CO desorption, followed by physical sputtering of residual carbon, iron, and rhenium atoms, broadly supporting the collision cascade model of deposition over the secondary electron model.[37]

In the present study, we have examined the sequence of surface reactions that accompany the interactions of low-energy (860 eV) Ar^+ ions with nanometer-thick films of three organometallic precursors under UHV conditions using *in situ* X-ray photoelectron spectroscopy (XPS) to observe changes in bonding and chemical composition within the adsorbate layer and mass spectrometry (MS) to identify volatile species produced during ion bombardment. The three precursors, $Ru(CO)_4I_2$, $Co(CO)_3NO$, and $WN(NMe_2)_3$, have different metal centers and different ligand types (Chart 1). This allows

Chart 1. Structures of the Three Organometallic Precursors Used in This Study

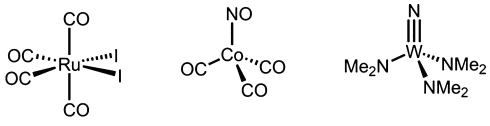

$Ru(CO)_4I_2$ $Co(CO)_3NO$ $WN(NMe_2)_3$

us to study how organometallic structure determines reactivity and to elucidate the sequence of elementary reaction steps that accompany ion−molecule interactions. Ion-induced reactions are discussed in terms of not only the deposition processes and associated bond-breaking events but also the balance between deposition and sputtering. Further, we compare our results to studies of the low-energy (500 eV) electron-induced decomposition of the same precursors and consider our results in the broader context of various FIBID deposition models.

METHODS

Synthesis. *General.* Unless otherwise stated, all reactions were carried out under an inert atmosphere (N_2) using standard Schlenk techniques. Unless otherwise specified, all reagents were purchased from Sigma-Aldrich and used without further purification. Solvents were purified using a MBraun MB-SP solvent purification system and stored over 4 Å molecular sieves. $Ru(CO)_4I_2$ was synthesized as described in the literature[38−40] and characterized by comparison to literature data.[38,39] $WN(NMe_2)_3$ was synthesized according to established literature methods.[41−43] $Co(CO)_3NO$ was purchased from Strem Chemicals.

Surface Science Experiments. *General.* All surface science experiments were performed in an UHV chamber equipped with an X-ray photoelectron spectrometer (PHI 5400 with Mg Kα anode), quadrupole mass spectrometer (QMS, Balzers Prisma QMA 200), flood electron gun, and ion gun.[44−46] Precursors were placed in glass fingers and attached to a UHV-compatible leak valve in a glovebox, which was then attached to the UHV chamber. $Ru(CO)_4I_2$ was heated to 40−45 °C and adsorbed onto a cooled gold substrate (polycrystalline Au foil) (−100 °C) to form ≈1.6 to 1.7 nm thin films. Polycrystalline Au foil was chosen for the surface science study because of its relative ease of cleaning, and there is no spectral overlap of Au($4f_{7/2}$) with any of the prominent Ru, Co, W, C, N, or O XPS transitions. $Co(CO)_3NO$ was dosed at room temperature onto a cooled gold substrate (−130 °C) and formed thin films of ≈1.1−1.4 nm thickness. $WN(NMe_2)_3$ was heated to 80−85 °C and adsorbed onto a cooled gold substrate (−100 °C) to form ≈1.5 to 2.0 nm thin films. For each precursor, film thickness was determined by measuring the attenuation of the Au(4f) substrate signal upon adsorption.[44−46] During XPS analysis and ion bombardment, substrate temperatures were held constant at the same temperature used for precursor adsorption (±5 °C) to avoid any complications from thermal effects. Previously published control studies on the effects of X-ray irradiation on $Ru(CO)_4I_2$ and $Co(CO)_3NO$ films demonstrated that changes to the XPS spectral profiles caused by X-ray irradiation occur at a much slower rate than those caused by Ar^+ exposure; thus, all experimentally observed changes are associated with Ar^+ exposure.[33,34,47,48] For $WN(NMe_2)_3$, the effect of X-ray irradiation was assessed as part of this investigation and is discussed in the Results and Discussion section pertaining to $WN(NMe_2)_3$. Both the Ar^+ and electron beams were defocused to ensure that the entire 1 cm^2 substrate surface was exposed to ions or electrons, respectively. Mass spectra could not be acquired during Ar^+ bombardment of $WN(NMe_2)_3$ because of fouling of the QMS filament by the precursor.

Ion Bombardment. Ion bombardment was performed using a PerkinElmer PHI model 04-303 differentially pumped ion gun with a primary Ar^+ beam energy of 880 eV and a substrate bias of +20 eV (to prevent the escape of secondary electrons), giving a relative beam energy of 860 eV. The ion beam was at ≈45° with respect to the surface normal, giving a beam energy of approximately 600 eV along the surface normal. The primary ion current density for the experiments performed on $Ru(CO)_4I_2$ and $WN(NMe_2)_3$ was calculated to be ≈40 nA/cm^2 while that for the experiments performed on $Co(CO)_3NO$ was ≈70 nA/cm^2.

Electron Irradiation. Electron irradiation was performed using a Specs FG 15/40 commercial flood gun with an incident electron energy of 500 eV, calculated from the energy of the flood gun (480 eV) and the substrate bias (+20 eV). The sample was rotated during electron irradiation so that the electron beam was incident along the surface normal. Electron flux is reported in terms of dose (e^-/cm^2; 1 × 10^{17} e^-/cm^2 = 1.6 mC/cm^2).

RESULTS AND DISCUSSION

$Ru(CO)_4I_2$. Figure 1 depicts the evolution of XPS spectra for the C(1s)/Ru(3d), O(1s), and I($3d_{5/2}$) regions of $Ru(CO)_4I_2$ films with increasing ion beam exposure dose. The spectra of the nanometer-thick $Ru(CO)_4I_2$ molecular film before ion beam exposure are depicted in each region (Ar^+ ion dose = 0 mC/cm^2).

To make a clear comparison between the C(1s) and Ru(3d) peaks (which overlap), the spectra have been deconvoluted. Before ion beam exposure, there are four peaks in the C(1s)/Ru(3d) region centered at 294.4, 289.2, 287.4, and 283.2 eV. The two higher binding energy peaks (depicted in blue in Figure 1a) at 289.2 and 294.4 eV can be attributed to the C(1s) peak and the $\pi-\pi^*$ transition (barely visible in Figure 1a) of the CO ligand associated with metal carbonyls, respectively.[49,50] The two lower binding energy peaks at 283.2 and 287.4 eV (depicted in red) are assigned to the Ru($3d_{5/2}/3d_{3/2}$) doublet associated with molecular Ru-

https://dx.doi.org/10.1021/acs.jpcc.0c07269
J. Phys. Chem. C 2020, 124, 24795−24808

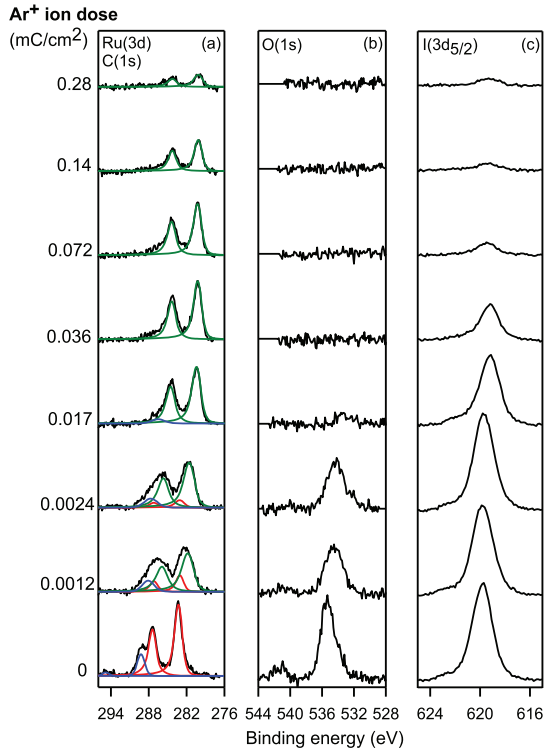

Figure 1. Evolution of the C(1s)/Ru(3d), O(1s), and I($3d_{5/2}$) XPS regions for ≈1.6−1.7 nm films of $Ru(CO)_4I_2$ adsorbed onto a Au substrate at −100 °C and exposed to increasing dose of Ar^+ ions. The C(1s)/Ru(3d) region is fit to show contributions clearly from the carbonyl carbon (blue), the initial Ru species (red), and the final Ru species (green).

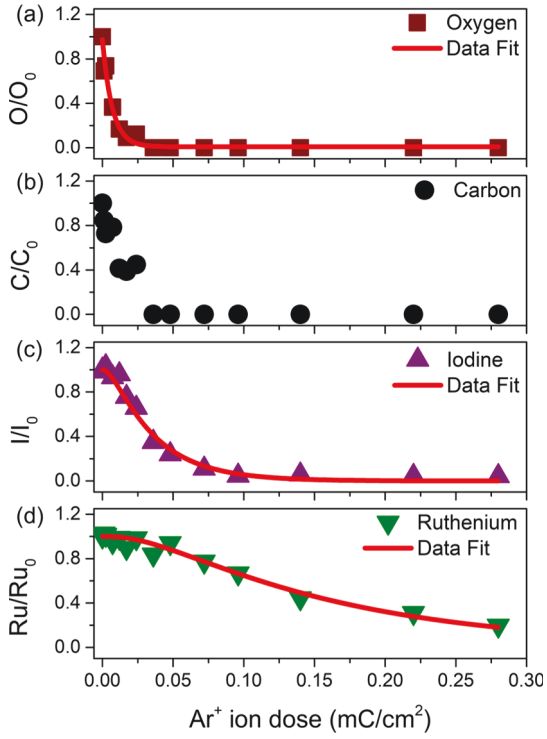

Figure 2. Change in fractional coverage of O, C, I, and Ru atoms as a function of increasing Ar^+ dose. The graphs (a,c,d) were fit by the integrated rate functions shown in eqs 2, 4, and 6, respectively.

$(CO)_4I_2$.[51,52] The O(1s) region initially has two peaks: a large peak centered at 535.2 eV and a smaller peak centered at 541.5 eV. The larger peak is attributed to the CO ligand, while the smaller peak is a $\pi-\pi^*$ shake up feature. Prior to ion beam exposure, the I($3d_{5/2}$) region consists of a single peak, centered at 619.8 eV (see Figure 1b).[53−56]

As a consequence of ion beam exposure, there is a significant decrease in the intensities of the two peaks associated with the initial Ru species (shown in red in Figure 1a) and a concurrent growth in two peaks centered at 281.7 and 285.9 eV (shown in green in Figure 1a). These new peaks are assigned, respectively, as the Ru($3d_{5/2}$) and Ru($3d_{3/2}$) peaks associated with the species produced by ion bombardment. The intensities of the peaks associated with the product Ru species remain relatively constant up to 0.036 mC/cm^2 but decrease in intensity for larger ion doses. The C(1s) peak intensity rapidly decreases upon ion irradiation; after an ion dose of 0.036 mC/cm^2, no C(1s) peak is visible.

In the O(1s) region, ion beam exposure produces a rapid decrease in oxygen atom coverage. For ion doses higher than 0.036 mC/cm^2, there is no observable oxygen remaining. In the I($3d_{5/2}$) region, ion exposure initially has little effect, but Ar^+ doses higher than ≈0.024 mC/cm^2 cause the intensity of the iodine peak to decrease systematically. Minimal iodine is observed at ion doses higher than 0.072 mC/cm^2.

The solid symbols in Figure 2 represent the variation in the integrated spectral intensity within the C(1s), Ru(3d), O(1s), and I($3d_{5/2}$) regions as a function of ion beam exposure dose. Each data point represents the integrated XPS spectra for the respective element after a period of ion beam bombardment, normalized to the value measured for the unexposed $Ru(CO)_4I_2$ film. As can be seen in Figure 2a,b, the initial effect of Ar^+ bombardment is to remove all oxygen and carbon atoms from the surface. This change occurs over the same regime as the reduction in binding energy in the Ru XPS but does not lead to any change in the Ru or I atom coverage. Thus, after an ion dose of 0.0024 mC/cm^2, analysis of Figure 2a and b shows that the coverage of C and O atoms has all but disappeared, while Ru and I coverages are left unchanged from their initial values. For ion doses between 0.024 and 0.072 mC/cm^2, the dominant change is iodine loss, followed by the loss of Ru atoms at ion doses in excess of 0.072 mC/cm^2.

Figure 3 demonstrates the normalized kinetics of CO desorption characterized by the MS signal at 12 amu (C^+, black solid line) overlaid with the fractional coverage of carbonyl ligands in the O(1s) XPS region (red boxes). Here, m/z = 12 was used to follow the CO desorption kinetics instead of m/z = 28 because the signal at m/z = 28 may also contain intensity from other species present (e.g., N_2). The inset in Figure 3 demonstrates that intact CO desorption accompanies ion bombardment. At an ion exposure dose of 0.00008 mC/cm^2, the only significant MS peaks detected are those associated with Ar^+ (m/z = 40), Ar^{2+} (m/z = 20), and CO (m/z = 28, 16, and 12, corresponding to CO, O, and C, respectively).

Upon low Ar^+ exposure (ion doses < 0.036 mC/cm^2), the initial Ar^+-induced process is the decomposition of $Ru(CO)_4I_2$, leading to the dissociation and desorption of all the four CO ligands.

$$Ru(CO)_4I_{2(ads)} + 860\ eV\ Ar^+_{(g)} \xrightarrow{\sigma_1} RuI_{2(ads)} + 4CO_{(g)}\uparrow \quad (1)$$

The assertion that all four CO ligands desorb intact is supported by the correlation between the CO desorption

https://dx.doi.org/10.1021/acs.jpcc.0c07269
J. Phys. Chem. C 2020, 124, 24795−24808

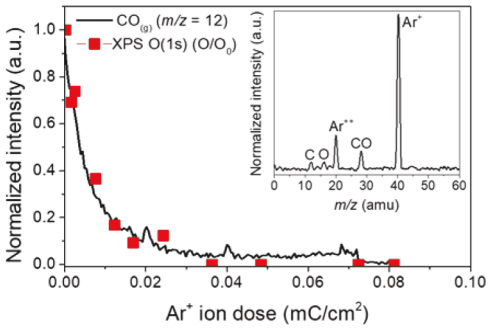

Figure 3. Kinetics of CO [followed using m/z = 12 amu (C^+)] desorption from an adsorbed $Ru(CO)_4I_2$ film and its correlation with the fractional coverage of O atoms as observed by XPS. MS and XPS signals were both normalized to their values at the onset of ion bombardment. The inset shows the mass spectrum of species desorbing from the $Ru(CO)_4I_2$ film after 0.00008 mC/cm^2 of ion beam bombardment.

kinetics and the loss of all oxygen atoms from the surface, as well as the desorption of intact CO observed by MS (Figures 3, S1, and S2). The fractional coverage of oxygen was chosen to measure the CO coverage rather than that of carbon because of the higher relative sensitivity of the O(1s) signal as compared to the C(1s) signal as well as the overlap between the $Ru(3d_{3/2})$ and C(1s) peaks, which produces greater error in the quantification of the C atom coverage. Interestingly, this ion-induced decomposition step occurred in the absence of any ion-induced desorption of the precursor (molecular sputtering), as can be seen by the lack of Ru desorption in this regime (Figure 2). Moreover, it should be noted that the decrease in the binding energy of Ru atoms observed by XPS that accompanies CO desorption (Figure S3) is consistent with the electronic changes at the metal center upon removal of the backbonding to the π-acid CO ligands.

The cross section of ion-induced $Ru(CO)_4I_2$ decomposition (σ_1) can best be determined by fitting the loss of oxygen signal to a first-order decay function

$$\frac{O_d}{O_0} = e^{-\sigma_1 d} \tag{2}$$

Here, σ_1 is the decomposition cross section, d is the ion dose, O_d is the oxygen coverage at dose d, and O_0 is the oxygen coverage at d = 0 mC/cm^2. This equation was fit to the O(1s) coverage, as shown in Figure 2a, and the cross section (σ_1) was found to be 2.3×10^{-15} cm^2 (R^2 = 0.99).

For Ar^+ ion exposures between ≈0.036 and 0.072 mC/cm^2, all CO has desorbed and iodine sputtering almost exclusively dominates, as can be seen in Figures 1 and 2. Consequently, after an Ar^+ dose of 0.072 mC/cm^2, Ru is effectively the only species remaining in the deposit (≈90 at. % Ru) with a coverage almost unchanged from its initial value. This second reaction step can therefore be described as

$$RuI_{2(ads)} + 860\ eV\ Ar^+_{(g)} \xrightarrow{\sigma_2} Ru_{(ads)} \tag{3}$$

This reaction is not intended to show the form of the sputtered iodine species but rather to reflect the effect of Ar^+ exposure.

Based on eqs 1 and 3, the decrease in iodine atom coverage occurs only after the formation of RuI_2; thus, the loss of iodine may be described by the following equation

$$\frac{I_d}{I_0} = \frac{\sigma_2 e^{-\sigma_1 d} - \sigma_1 e^{-\sigma_2 d}}{\sigma_2 - \sigma_1} \tag{4}$$

where I_d is the iodine coverage at dose d, I_0 is the iodine coverage at d = 0 mC/cm^2, σ_1 is the decomposition cross section for eq 1 (228.8×10^{-17} cm^2), σ_2 is the decomposition cross section for eq 3, and d is the Ar^+ dose.

Results of the data analysis using this fitting procedure are shown as the solid red line in the iodine region of Figure 2, wherein σ_2 was determined to be 50.1×10^{-17} cm^2 (R^2 = 0.99). Notably, this fitting accounts for the slight delay in the loss of iodine for small Ar^+ doses (<0.010 mC/cm^2) because of the prerequisite of RuI_2 formation.

For higher ion exposure doses (≥0.072 mC/cm^2), where all of the CO ligands have desorbed and most of the iodine has been sputtered, ruthenium sputtering occurs (Figure 1a,d). This process can be described by eq 5 (Note: Because the volatile ruthenium and iodine species have not been determined, they have been omitted and the reaction is therefore not balanced):

$$Ru_{(ads)} + 860\ eV\ Ar^+_{(g)} \xrightarrow{\sigma_3} \text{clean substrate} \tag{5}$$

Here, σ_3 is the decomposition cross section associated with eq 5. The integrated rate function for coverage of Ru atoms can therefore be written as

$$\begin{aligned}\frac{Ru_d}{Ru_0} = &\left(\frac{\sigma_1\sigma_2}{(\sigma_2-\sigma_1)(\sigma_3-\sigma_1)}\right)e^{-\sigma_1 d} \\ &+ \left(\frac{\sigma_1\sigma_2}{(\sigma_1-\sigma_2)(\sigma_3-\sigma_2)}\right)e^{-\sigma_2 d} \\ &+ \left(\frac{\sigma_1\sigma_2}{(\sigma_1-\sigma_3)(\sigma_2-\sigma_3)}\right)e^{-\sigma_3 d} \\ &+ \left(\frac{\sigma_2 e^{-\sigma_1 d} - \sigma_1 e^{-\sigma_2 d}}{\sigma_2-\sigma_1}\right)\end{aligned} \tag{6}$$

Here, Ru_d is the ruthenium coverage at dose d, Ru_0 is the ruthenium coverage at d = 0 mC/cm^2 dose, σ_1 is the cross section for eq 1 (228.8×10^{-17} cm^2), σ_2 is the cross section for eq 3 (50.1×10^{-17} cm^2), σ_3 is the cross section for eq 5, and d is the Ar^+ dose. This function (eq 6) was fit to the Ru coverage data in Figure 2d and the results are shown as a solid red line, giving a cross section (σ_3) of 1.2×10^{-16} cm^2 (R^2 = 0.98). This model provides a rationale for the clearly visible delay in the onset of Ru loss observed experimentally in Figures 1 and 3. In addition to providing a viable kinetic model to explain the experimental data, the cross sections indicate that the rate of the initial ion-induced decomposition of the $Ru(CO)_4I_2$ precursor leading to CO loss is about 5 times faster than the physical sputtering of I from RuI_2, which in turn is itself about 5 times faster than the rate of Ru sputtering.

Comparison with Electron-Induced Surface Reactions. An analogous UHV surface science approach has also recently been used to elucidate the reactions between $Ru(CO)_4I_2$ and low-energy electrons (500 eV). Results from these studies revealed that electron exposure produced an initial loss of two CO ligands.[48] This was contextualized as the initial step leading to deposition in FEBID, with the remaining two CO ligands desorbing from the partially decarbonylated intermediate at a much slower rate.[48] Comparing the two results,

https://dx.doi.org/10.1021/acs.jpcc.0c07269
J. Phys. Chem. C 2020, 124, 24795−24808

the electron-induced decomposition of adsorbed $Ru(CO)_4I_2$ clearly differs from Ar^+-induced decomposition; electron exposure produced an initial loss of only two CO ligands, while all four CO ligands were lost in the first Ar^+-induced ligand dissociation step. Additionally, the Ar^+-induced ligand dissociation reaction proceeds much faster than the initial electron-induced CO loss step, which was found to be complete after an electron dose of 1.6 mC/cm^2, while the initial ion-induced CO loss step (eq 1) is complete after an ion dose of 0.036 mC/cm^2.

$Co(CO)_3NO$. Figure 4 shows the XPS spectra of the C(1s), O(1s), N(1s), and $Co(2p_{3/2})$ regions of $Co(CO)_3NO$ films

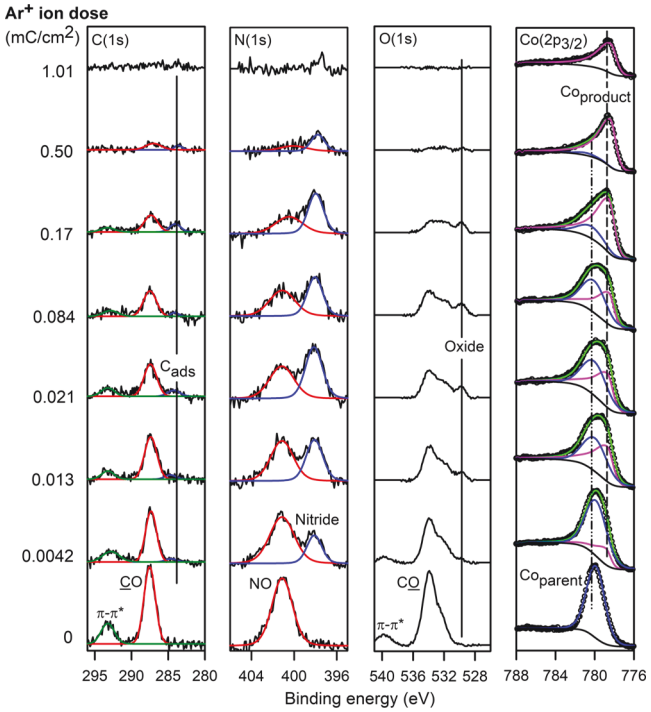

Figure 4. XPS spectra of the C(1s), N(1s), O(1s), and $Co(2p_{3/2})$ regions of adsorbed ≈1.1−1.4 nm thick $Co(CO)_3NO$ films as a function of increasing 860 eV Ar^+ bombardment (bottom to top). The C(1s), N(1s), and $Co(2p_{3/2})$ regions show peak deconvolutions, explained in the text. The Shirley background is shown in the $Co(2p_{3/2})$ region, as well as the envelope (sum of the fits, light green) and the raw intensity (black circles).

(≈1.1−1.4 nm) before (0 mC/cm^2) and after exposure to increasing doses of 860 eV Ar^+ ions. In the C(1s) region, a nonlinear background was observed and subtracted from the C(1s) spectra, as illustrated in Figure S4.

Prior to Ar^+ bombardment, the C(1s) region consists of two peaks: a prominent peak centered at 287.5 eV (depicted in red) associated with the CO ligands and a smaller second peak centered at 293.1 eV (shown in green) associated with the $\pi-\pi^*$ (shake-up) transition common in transition metal carbonyls.[54,57] The pristine N(1s) region exhibits a single peak at 401.1 eV (shown in red) assigned to the NO ligand.[47] In the O(1s) region, two peaks exist prior to ion bombardment: a dominant peak centered at 534.0 eV that has contributions from both the CO and NO ligands[47] and a smaller peak at 539.9 eV associated with a $\pi-\pi^*$ transition[54] common to both CO and NO ligands. The unexposed $Co(2p_{3/2})$ region exhibits a single peak at 780.0 eV (depicted in blue) along with a Shirley background (depicted in black) typical for transition metal XPS transitions.[34,47,58]

Following Ar^+ exposure, both the CO and $\pi-\pi^*$ peaks in the C(1s) region decrease in intensity and a small new peak appears at 284.7 eV (blue curve), assigned to graphitic carbon (C_{ads}). The intensity of this peak grows until an Ar^+ dose of 0.17 mC/cm^2 but decreases thereafter. After an Ar^+ dose of 1.01 mC/cm^2, no detectable carbon remains on the surface. In the N(1s) region, Ar^+ exposure produces a decrease in the intensity of the NO feature and a simultaneous growth of a new peak at 398.1 eV (depicted in blue), assigned to a nitride species,[34,59] whose intensity continuously increases for Ar^+ doses <0.021 mC/cm^2; at larger ion doses, this peak decreases in intensity. Similar to the C(1s) region, almost no nitrogen atoms are observed on the surface after an Ar^+ dose of 1.01 mC/cm^2. Upon Ar^+ exposure, the O(1s) region is dominated by a loss of intensity for all peaks (CO, NO, and shake-up), with a simultaneous growth of a small peak at 529.8 eV associated with an oxide.[60] Similar to the nitride peak in the N(1s) region, the oxide peak grows in intensity for an Ar^+ dose of 0.17 mC/cm^2, after which it decreases in intensity. At an Ar^+ dose of 1.01 mC/cm^2, all oxygen has been removed from the surface.

Argon ion exposure causes the $Co(2p_{3/2})$ peak to broaden and shift to lower binding energy. The overall peak profile can be fit by two components: one associated with the parent molecule (blue) with peak at 779.9 eV, which decreases in intensity with Ar^+ bombardment, and a new species with a binding energy of 778.6 eV that initially increases in intensity

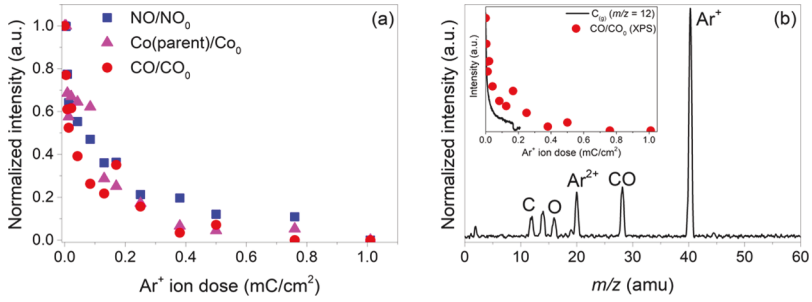

Figure 5. (a) Fractional coverage of NO (blue filled squares), CO (red filled circles), and parent Co species as measured by XPS, plotted as a function of Ar^+ dose. (b) Mass spectrum of fragments desorbing from a film of $Co(CO)_3NO$ measured after an Ar^+ dose of 0.015 mC/cm^2. The peak at m/z = 14 is considered a background peak as it does not change in intensity when the ion gun is turned off (see Figure S5). The inset shows the kinetics of gas-phase CO desorption from an adsorbed $Co(CO)_3NO$ film during Ar^+ bombardment as measured by the m/z = 12 ($C_{(g)}$) MS peak (black line) overlaid with the fractional coverage of CO as measured by the respective C(1s) XPS peak (red filled circles).

https://dx.doi.org/10.1021/acs.jpcc.0c07269
J. Phys. Chem. C 2020, 124, 24795−24808

with Ar^+ bombardment (depicted in pink in Figure 4). The binding energy and shape of this new peak is similar to those of both metallic cobalt and cobalt nitride, which have similar binding energies and peak shapes, and the peak shape was deconvoluted by using the standard asymmetric peak shape (LA(1.2,5,5)) described for the cobalt metal sample.[58,61] Analysis of the Co($2p_{3/2}$) region reveals that the product species continues to increase in intensity for an Ar^+ dose of 0.17 mC/cm^2 but decreases thereafter, albeit at a slower rate than the loss of C, O, and N species. After an ion dose of 1.01 mC/cm^2, aside from a small amount of residual nitrogen, the only species remaining on the surface is the cobalt species produced by Ar^+ bombardment.

In Figure 5a, the fractional coverage of NO (blue solid squares), CO (red solid circles), and parent Co (pink solid triangles) species, as measured by their respective N(1s), C(1s), and Co($2p_{3/2}$) XPS profiles, is plotted as a function of Ar^+ dose. As can be seen in Figure 5a, the loss of CO, NO, and the parent Co species follow the same dependence on Ar^+ exposure. In Figure 5b, the mass spectrum of fragments desorbing from the $Co(CO)_3NO$ film after an Ar^+ exposure of ≈0.015 mC/cm^2 is shown. The only significant MS peaks detected are those associated with Ar^+ (m/z = 40), Ar^{2+} (m/z = 20), and CO (m/z = 28, 16, and 12 corresponding to CO, O, and C, respectively). The peak at m/z = 14 is identified as a background peak as described in Figure S5. Thus, CO is the only ligand observed to desorb during ion bombardment. The lack of NO desorption is most clearly evidenced by the absence of a peak at m/z = 30, the dominant peak in the electron impact ionization MS of NO.[62] The inset in Figure 5b shows the normalized kinetic trace of CO desorption (as measured by m/z = 12, C^+) during Ar^+ bombardment of a $Co(CO)_3NO$ film overlaid with the fractional coverage of CO remaining on the surface (as measured in Figure 4 by the C(1s) peak associated with CO). As shown in Figure 5b (inset), the rate of CO desorption is qualitatively similar to the loss of CO from the surface (red dots) as measured by XPS.

Figure 6a depicts the changes in fractional coverage of graphitic carbon, oxide, and nitride species as a function of Ar^+ dose. To facilitate a direct comparison, all of the data points in Figure 6 were normalized to the maximum XPS intensity observed for each species. Prior to ion irradiation, there is no detectable coverage of any of these three species on the surface. As can be seen in Figure 6a, the relative coverage of each of these species follows a similar profile, increasing in intensity upon ion irradiation until a peak is reached between 0.05 and 0.2 mC/cm^2, decreasing thereafter. In Figure 6b, the variation in the total Co atom coverage (pink open triangles) is plotted along with the contribution from the Co species produced by ion irradiation (purple filled inverted triangles). In the initial stages of Ar^+ exposure (<0.2 mC/cm^2), the product Co species grows in intensity without any loss of Co atoms from the surface. This occurs over a similar ion dose regime to the loss of the NO and CO groups (Figure 5) and the growth of the oxide, nitride, and graphitic carbon species (Figure 6). At higher Ar^+ doses (>0.2 mC/cm^2), Co is seen to be lost from the surface, albeit at a slower rate than that of graphitic carbon, oxide, and nitride species.

Analysis of Figures 4–6 demonstrates that the Ar^+-induced reactions of adsorbed $Co(CO)_3NO$ occur via two sequential steps. The first step predominates at ion doses <0.2 mC/cm^2 and involves the ion-induced decomposition of adsorbed $Co(CO)_3NO$. This initial step is characterized by loss of the

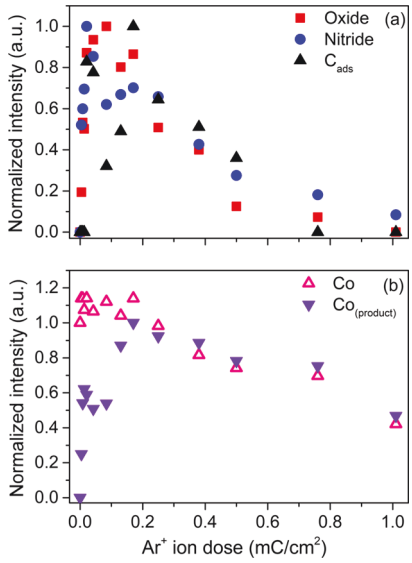

Figure 6. Changes in the coverage of (a) oxide (red filled squares), nitride (blue filled circles), and C_{ads} (black filled triangles) species and (b) total Co (pink open triangles) and product Co species (purple filled inverted triangles) as a function of increasing Ar^+ dose. In (a), signal intensities have been normalized to the maximum values observed during ion bombardment to make their temporal evolution clearer and while in (b), signal intensities have been normalized to the Co signal observed prior to ion bombardment.

CO, NO, and parent Co species (Figures 4 and 5a). Each of these species follows a similar kinetic loss profile (Figure 5a), indicating that each process is correlated with the other. Analysis of Figures 4 and 6 shows that during this same regime, there is a concurrent formation of nitride and product Co species, along with the formation of smaller fractional coverages of oxide and graphitic carbon; each of these three species also follows a similar kinetic profile to one another.

Figure S6 shows that on average, each $Co(CO)_3NO$ molecule decomposes to form 0.22 graphitic carbon (C_{ads}) atoms and 0.26 oxide ions. Because of the similarity in the coverage of graphitic carbon and oxide species, coupled with the overlap in their intensity profiles (Figure S6), it seems likely that these species originate from the decomposition of a small fraction of the CO ligands. This agrees with the XPS (Figure 5a) and MS data (Figure 5b), which indicate that the overwhelming majority (>90%) of the CO ligands desorb intact. In contrast, the N(1s) region indicates that during precursor decomposition, the NO ligands undergo stoichiometric conversion to yield a cobalt nitride species in the absence of any NO desorption. However, analysis of the change in total coverage of oxygen during $Co(CO)_3NO$ decomposition indicates that oxygen atoms in the NO ligands desorb (presumably as ROS) rather than being incorporated into the deposit.

The initial step of ion-induced decomposition of $Co(CO)_3NO$ can therefore be summarized as

$$Co(CO)_3NO + Ar^+ \rightarrow CoN(O_{x(ads)}) + (3 - x)CO_{(g)} + ROS + xC_{(graphitic)} \qquad (x \approx 0.25) \quad (7)$$

Interestingly, despite the significant energy being imparted to the adsorbate by the ion beam, no ion-induced molecular desorption is observed as evidenced by the lack of Co desorption (Figure 6b) during the precursor decomposition.

https://dx.doi.org/10.1021/acs.jpcc.0c07269
J. Phys. Chem. C 2020, 124, 24795–24808

This selectivity for CO desorption over NO desorption upon Ar^+ bombardment may be a consequence of the low metal−carbonyl bond dissociation energies (BDEs), in comparison to metal−nitrosyl BDEs, because of the stronger backbonding behavior of the nitrosyl group.[63,64] For $Co(CO)_3NO$, BDEs for the Co−CO and Co−NO ligands were calculated to be 1.26−1.42 and 1.63−1.70 eV, respectively.[64,65] Further, the internal BDE for C≡O is 11.08 eV, higher than the 7.5 eV for N≡O bonds.[66] Interestingly, this selectivity for CO desorption over NO desorption has also been previously observed in both electron-induced[34] and CVD[67] reactions of $Co(CO)_3NO$.

The second Ar^+-induced reaction step, which predominates at ion doses >0.2 mC/cm^2, is characterized by physical sputtering of the oxide, graphitic carbon, and nitride species produced by the ion-induced decomposition of $Co(CO)_3NO$, along with a slower sputtering of the cobalt atoms associated with the cobalt nitride (Figures 4 and 6). This can be expressed as eq 8 (Note: Because the nature of volatile carbon, oxygen, and nitrogen species removed by sputtering is not determined, they have been omitted and the reaction is therefore not balanced)

$$CoN(O_{x(ads)}) + xC_{(graphitic)} + Ar^+ \rightarrow Co_{(ads)} \quad (x \approx 0.25) \tag{8}$$

Figure 6 shows that the sputter rates of the ligand-derived species (C, O, and N) are all similar to one another but about 2.6 times higher than that of the product cobalt atoms.

Overall, the Ar^+-induced reactions of adsorbed $Co(CO)_3NO$ can be described by an initial decomposition step (eq 7), which leads to the loss of most of the CO ligands (≈2.75) with the residual CO ligands decomposing into graphitic carbon and oxide, accompanied by complete decomposition of the NO ligands into adsorbed nitride and ejected oxygen. This is followed by a second step (eq 8) characterized by sputtering of the residual C, O, and N species at a faster rate than that of Co. Qualitatively, this sequence of reaction steps helps to rationalize the ≈50 at. % Co in FIBID nanostructures created from $Co(CO)_3NO$,[25] despite the presence of only ≈10 at. % Co in the precursor.

Comparison with Electron-Induced Surface Reactions. A previous study of the electron-induced decomposition of adsorbed $Co(CO)_3NO$ by Rosenberg et al. showed that electron-induced reactions also proceeded in two steps: an initial desorption of half of the CO ligands ($x \approx 1.5$) accompanied by decomposition of the NO group and the formation of a cobalt oxynitride. The residual CO groups decomposed under the influence of further electron beam irradiation, further oxidizing the cobalt atoms.[34] This is substantially different from the Ar^+-induced reactions seen here, wherein almost all of the CO ligands (≈2.75) desorb in the initial step, while decomposition of NO is accompanied by the formation of cobalt nitride and ejection of the oxygen atoms.

$WN(NMe_2)_3$. Figure 7 shows the evolution of the C(1s), N(1s), and W(4f) XPS regions of a thin film (≈1.2 nm) of $WN(NMe_2)_3$ bombarded with 860 eV Ar^+ ions. Any effects of X-ray irradiation during XPS analysis on the $WN(NMe_2)_3$ film are anticipated to be similar to those of electron irradiation, as has been shown in previous studies.[33] Because no changes in either composition or XPS peak positions are observed upon 500 eV electron irradiation of $WN(NMe_2)_3$ thin films

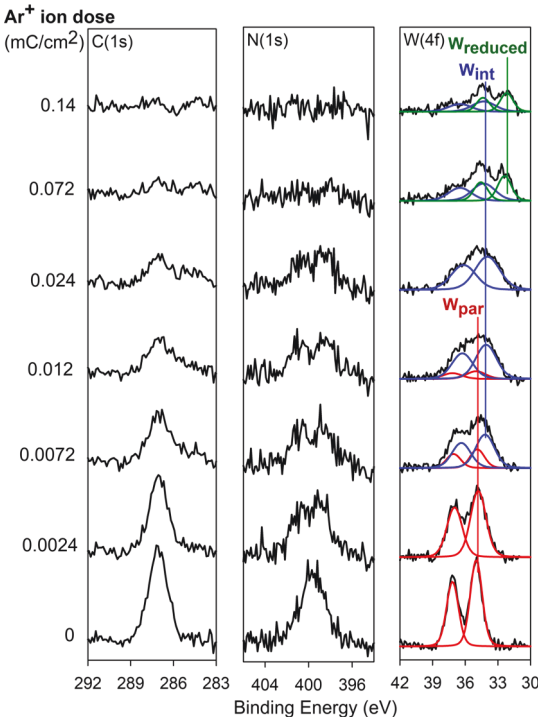

Figure 7. XPS spectra of the C(1s), N(1s), and W(4f) regions of a thin film (≈1.2 nm) of $WN(NMe_2)_3$ as a function of increasing 860 eV Ar^+ bombardment (bottom to top). The W(4f) peaks have been deconvoluted, as explained in the text.

(Supporting Information, Figure S7), the spectral changes observed in Figure 7 can be attributed solely to Ar^+ bombardment.

The spectra at the bottom of Figure 7 (ion dose = 0 mC/cm^2) show the as-deposited, unirradiated $WN(NMe_2)_3$ film. In these spectra, the C(1s) region consists of a single peak at 287.1 eV, assigned to the three NMe_2 ligands ($N(\underline{C}H_3)_2$).[68] The N(1s) region also consists of a single peak centered at ≈399.6 eV, likely a convolution of the nitrido nitrogen peak ($W\underline{N}(NMe_2)_3$)[69] and the dimethylamido nitrogen peak ($WN(\underline{N}Me_2)_3$).[68,69] In the W(4f) region, two peaks can be seen at 35.0 and 37.2 eV, respectively, corresponding to the W(4f$_{7/2}$) and W(4f$_{5/2}$) peaks associated with the parent compound and similar to previous values for W(VI) compounds.[70,71] These peaks have been deconvoluted and are shown as red curves in Figure 7, labeled "W_{par}".

Upon Ar^+ bombardment, the C(1s) peak decreases in intensity and broadens considerably; after an ion dose of 0.14 mC/cm^2, no carbon atoms remain. In the N(1s) region, increasing Ar^+ exposure also leads to a systematic decrease in spectral intensity, although the N(1s) peak broadens and splits into two differentiable peaks at ≈398.5 and 400.9 eV. We tentatively assigned the lower binding energy peak to the N species directly bonded to the W atom, with the higher binding energy being indicative of the formation of CN_x species.[43] After an Ar^+ dose of 0.14 mC/cm^2, the N(1s) peak cannot be discerned from the baseline.

The most significant spectral changes due to Ar^+ bombardment appear in the W(4f) region. Within the first 0.0072 mC/cm^2 of Ar^+ exposure, the W(4f) peaks associated with the parent $WN(NMe_2)_3$ broaden substantially and the W(4f) profile shifts to lower binding energy. The resultant W(4f) spectral envelope can be fit by a combination of the parent W

https://dx.doi.org/10.1021/acs.jpcc.0c07269
J. Phys. Chem. C 2020, 124, 24795−24808

compound and a new species with W($4f_{7/2}$)/W4f($_{5/2}$) peaks at ≈34.2 and 36.4 eV, respectively (blue curves in Figure 7), indicative of an intermediate tungsten species (labeled "W_{int}" in Figure 7) with a binding energy similar to tungsten carbonitride (WN_xC_y) species produced during CVD from $WN(NMe_2)_3$.[41] Continued Ar^+ irradiation (>0.0072 mC/cm^2) causes the W(4f) peaks associated with the intermediate (W_{int}) to continue to increase in intensity while the peaks associated with the parent compound (W_{par}) disappear. After an Ar^+ dose of 0.072 mC/cm^2, a second new W species (green curves in Figure 7) appears with W($4f_{7/2}$) and W($4f_{5/2}$) peaks at ≈32.4 and 34.6 eV, respectively, associated with a highly reduced form of tungsten (labeled "$W_{reduced}$" in Figure 7).[33] Further Ar^+ exposure leads predominantly to an overall decrease in spectral intensity within the W region, with both the intermediate and highly reduced forms of W present. After an Ar^+ dose of 0.14 mC/cm^2, the highly reduced W species has a W($4f_{7/2}$) binding energy of 32.2 eV, approaching the value of bulk metallic tungsten [W($4f_{7/2}$) = 31.4].[57]

Figure 8a shows the relative coverage of carbon (red filled circles) and nitrogen (red open inverted triangles) as a function of Ar^+ dose, as well as the change in the thickness of the adsorbate film (blue filled squares). The total carbon and nitrogen coverages both show a very similar dependence on Ar^+ dose to that of the film thickness, with an approximate 70% decrease during the initial ≈0.08 mC/cm^2 of Ar^+ exposure. Conversely, the total tungsten coverage (Figure 8b) remains relatively constant (≈20% loss) during this period.

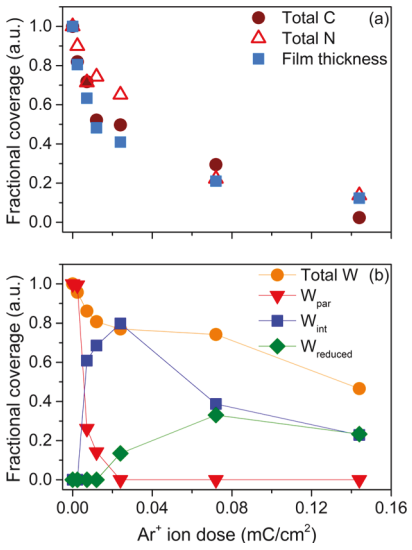

Figure 8. Relative coverage of (a) carbon (dark red filled circles), nitrogen (red open inverted triangles), and film thickness (blue filled squares) and (b) tungsten (orange circles) and the tungsten speciation shown in Figure 7: W_{par} (red inverted triangles), W_{int} (blue squares), and $W_{reduced}$ (green diamonds) upon exposure to 860 eV Ar^+. The lines in (b) are not intended to imply any fit but rather are meant to guide the eye.

Figure 8b shows the relative coverage of tungsten (orange filled circles), as well as the three tungsten species identified in Figure 7: the parent compound (W_{par}, red filled inverted triangles), the intermediate species (W_{int}, blue filled squares), and the highly reduced species ($W_{reduced}$, green filled diamonds). Ar^+ exposure is seen to cause a rapid conversion of $WN(NMe_2)_3$ into the intermediate WN_xC_y species. At an Ar^+ dose of about 0.02 mC/cm^2, none of the parent tungsten species remains on the surface. For Ar^+ doses >0.02 mC/cm^2, the reduced tungsten species appears, comprising about 40% of the initial tungsten signal after about 0.7 mC/cm^2 of Ar^+ exposure. At higher Ar^+ doses (>0.7 mC/cm^2), the conversion of the intermediate WN_xC_y species to the highly reduced form of W is accompanied by a measurable loss of tungsten atoms due to sputtering—about 50% of the initial tungsten coverage remains after an Ar^+ dose of 0.14 mC/cm^2.

As is evident in Figures 7 and 8, the initial effect of Ar^+ bombardment (<0.02 mC/cm^2) is the conversion of adsorbed $WN(NMe_2)_3$ to an intermediate tungsten species with a binding energy that supports the formation of a tungsten carbonitride (WN_xC_y) species. Indeed, after an Ar^+ dose of ≈0.02 mC/cm^2, the only tungsten species present on the surface is WN_xC_y. At this stage of the reaction, the N(1s) region contains two peaks, possibly because of the presence of WN_xC_y and CN_x species. Because Ar^+-induced formation of WN_xC_y is accompanied by the loss of about 40% of the C and N atoms (Figure 8a), this initial regime of ion-induced precursor decomposition can be represented as

$$WN(NMe_2)_{3(ads)} + Ar^+_{(g)}\,(860\ eV) \rightarrow WN_xC_{y(ads)} + CN_{x(ads)} \quad (9)$$

For Ar^+ doses of 0.02−0.08 mC/cm^2, the tungsten carbonitride (WN_xC_y) species begin to undergo further Ar^+-induced conversion to a reduced form of W ($W_{reduced}$), with a binding energy that approaches metallic tungsten. This process is not accompanied by any sputtering of W atoms (Figure 8b) but is accompanied by the loss of carbon and nitrogen at similar rates. Thus, this step can be qualitatively represented by

$$WN_xC_{y(ads)} + C_yN_{z(ads)} + Ar^+_{(g)}\,(860\ eV) \rightarrow W_{(reduced)} \quad (10)$$

We note here that, because the nature of the volatile carbon and nitrogen species removed by sputtering was not determined, they have been omitted and the reaction (eq 10) is therefore not balanced.

At higher Ar^+ doses (>0.08 mC/cm^2), this second reaction step competes with sputtering of the reduced tungsten species ($W_{reduced}$), leading to a decrease in the W atom coverage. The close correlation between film thickness and the coverage of C and N atoms supports the elementary reaction steps described in eqs 9 and 10.

Comparison with Electron-Induced Surface Reactions. In contrast to the effects of Ar^+ exposure, electron irradiation of adsorbed $WN(NMe_2)_3$ (Figure S7) produces only peak broadening in the C(1s), N(1s), and W(4f) regions; no carbon, nitrogen, or tungsten atoms are removed from the surface and the film thickness does not change over an electron dose of 54 mC/cm^2 (Figure S8). Given the known propensity for electron irradiation to induce hydrogen loss via C−H bond cleavage,[72−74] the overall effect of electron irradiation appears to be limited to the decomposition of the NMe_2 ligands into adsorbed nitrogen and carbon species, which can be represented by

$$WN(NMe_2)_{3(ads)} + e^- \rightarrow WN_xC_{y(ads)} + H_{2(g)} \quad (11)$$

https://dx.doi.org/10.1021/acs.jpcc.0c07269
J. Phys. Chem. C 2020, 124, 24795−24808

SUMMARY

The initial effect of Ar^+ ion bombardment upon each of the three precursors is to decompose the adsorbed molecular precursor into a metal-containing deposit (eqs 1, 7, and 9). For two of the three precursors [$Ru(CO)_4I_2$ and $Co(CO)_3NO$], this decomposition step is accompanied by desorption of all ($Ru(CO)_4I_2$) or most (>90%, $Co(CO)_3NO$) of the CO ligands with concomitant production of RuI_2 and CoN_x. Subsequently, the sputtering of iodine and nitride species leads to the reduction of the metals. A comparison of these results with the corresponding effects of low-energy electrons reveals that, although electron irradiation also leads to CO desorption from both precursors, the extent of CO desorption is measurably less extensive.[34,48] These differing effects of ion and electron beam irradiation on metal carbonyls mirror recent results obtained on a bimetallic organometallic complex, $CpFe(CO)_2Re(CO)_5$.[37] Despite the prevalence of CO desorption in the present investigation, a small amount of CO decomposition was observed during ion-induced decomposition of $Co(CO)_3NO$, resulting in production of graphitic carbon and a small degree of cobalt oxidation. In previous studies of low-energy electron reactions with organometallic precursors, formation of graphitic carbon and simultaneous metal oxidation has also been observed, although its formation was ascribed to the electron-stimulated decomposition of partially decarbonylated intermediates from the initial decomposition step.[33,34] In contrast, the ion-induced CO decomposition in $Co(CO)_3NO$ is correlated with precursor decomposition (compare Figures 5a and 6a). This suggests that it represents one possible decomposition pathway for the precursor, albeit with a significantly lower probability than CO loss. This reaction partitioning is analogous to the observation of a small number of C and O species in the ion-induced reactions of gas-phase $Fe(CO)_5$, which are also dominated by CO loss.[31]

In contrast to the almost complete desorption of CO ligands, the NO ligand in $Co(CO)_3NO$ undergoes stoichiometric decomposition as a consequence of ion bombardment, analogous to the effect of low-energy electrons.[34] Unlike the effect of low-energy electrons, however, ion-induced decomposition of NO causes desorption of all of the associated oxygen atoms to yield cobalt nitride, while electron-stimulated NO decomposition leads to oxynitridation of cobalt. Moreover, the selective nitridation of cobalt from NO decomposition upon ion beam exposure is opposite to the selective oxidation of cobalt, which is observed as a consequence of the thermal reactions of cobalt with NO.[34] Thus, the detailed reactions of the NO ligand appear to be highly dependent on the decomposition mechanism (electron vs ion vs thermal).

For $WN(NMe_2)_3$, ion-induced precursor decomposition does cause a partial reduction of the tungsten atoms; however, the nearly invariant W/N/C ratio during the initial stages of Ar^+ ion irradiation indicates that this is not accompanied by any ligand desorption but is rather likely driven by ion-induced C−H, N−H, and C−N bond cleavage. This process leaves nitrogen atoms still bonded to the tungsten atom, with Figures 7 and 8 suggesting the formation of a tungsten carbonitride (WN_xC_y) species. The absence of ligand desorption during both electron and ion-induced reactions with adsorbed $WN(NMe_2)_3$ is unusual for charged particle-induced decomposition of organometallic precursors. This behavior can reasonably be ascribed to the existence of strong covalent bonds between all of the ligands and the W atoms in $WN(NMe_2)_3$, such as the W≡N bond.[41,42] This implies that these ligands should therefore be avoided in the design of precursors for either FIBID or FEBID.

The mechanism responsible for precursor decomposition is assumed to be initiated by the formation of excited electronic states of the adsorbed precursor as a result of energy transfer from the incident ion.[31] Subsequent molecular decomposition occurs if these electronic states are dissociative or if the subsequent transfer of electronic energy to vibrational energy in turns leads to fragmentation. It should be noted that thermal effects are highly unlikely, given the low energy (860 eV) and flux (target current, <−100 nA/cm^2) of the incident ions. Indeed, we did not observe any increase in substrate temperature when the ion beam was incident upon a thermocouple attached to the backside of the sample holder. The detailed effects of ion-induced decomposition appear to be precursor-dependent; for example, in the case of $Ru(CO)_4I_2$, a single reaction channel, which leads to complete and exclusive CO desorption (eq 1), appears to dominate, in line with the relative BDEs (Ru−CO ≈ 1.5 eV; Ru−I ≈ 2.5 eV).[75,76] In comparison, for $Co(CO)_3NO$, the observation of both CO desorption and CO decomposition (eq 7) suggests the presence of multiple decomposition channels, analogous to the gas-phase behavior of $Fe(CO)_5$.[31] For all three precursors, the decomposition step differs from decomposition effected by low-energy electron irradiation. This supports the idea that ion-induced deposition is driven by ion−molecule interactions without a contribution from reactions associated with the low-energy electrons produced by the ion beam irradiation of the substrate/adsorbate. Moreover, the absence of significant molecular desorption, despite the fact that the precursor molecules are only bound to the surface by comparatively weak physisorption interactions, suggests that the ion energy is not only efficiently transferred into the precursor but also that the ensuing reactions of the precursor, which lead to decomposition, occur before energy is transferred to the adsorbate−substrate bond.

For all three precursors, the initial decomposition step is followed by ion-induced physical sputtering of the atoms in the deposit, in agreement with results obtained for $CpFe(CO)_2Re(CO)_5$.[37] In the case of $Co(CO)_3NO$, this includes the graphitic carbon, oxide, and nitride species produced during the decomposition of the parent compound. Regardless of the precursor's identity, it is apparent that the rates of sputtering for the ligand-derived contaminants in the deposit (C, N, O, and I) are larger than that of the respective metal atoms. Moreover, analysis of Figures 6a and 8a reveals that the organic contaminants are sputtered at similar rates to one another. As a consequence of the differential sputtering rates, the deposit contains almost exclusively metal atoms at the end of each of the experiments. The largely sequential nature of the decomposition and sputtering steps, coupled with the slower rates of metal atom sputtering, is most clearly evident for $Ru(CO)_4I_2$, where increasing Ar^+ doses lead to adsorbate layers composed first of Ru and I and then at higher ion doses composed almost exclusively of Ru (see Figure 1). For $Co(CO)_3NO$ and $Ru(CO)_4I_2$, physical sputtering does not lead to a measurable change in the binding energy of the metal atoms; in $Co(CO)_3NO$, this is a consequence of the similarity in binding energy and XPS profiles of CoN and Co, while for $Ru(CO)_4I_2$, it is a consequence of the similarity in electronegativities of Ru (2.2) and I (2.66). In contrast, for

https://dx.doi.org/10.1021/acs.jpcc.0c07269
J. Phys. Chem. C 2020, 124, 24795−24808

$WN(NMe_2)_3$, sputtering of the nitrogen atoms bound to W atoms leads to reduction and approaches the appearance of a metallic form of bulk W. Indeed, for $WN(NMe_2)_3$, it is the effects of ion-induced physical sputtering which produce the most profound changes and where the contrast between the ion- and electron-induced reactions is most apparent (compare Figures 7 and S7).

As discussed in the introduction, the mechanisms of ion beam-induced deposition are complex and varied. This is largely a consequence of the fact that when an energetic ion collides with a solid target, it undergoes both elastic and inelastic collisions with the atoms and electrons in the solid. This can in turn lead to numerous processes such as backscattering, sputtering, implantation, and ion-induced deposition of adsorbates. By studying the effects of ion exposure on 1−2 ML equivalence films of precursor molecules adsorbed onto chemically inert substrates, our study provides information primarily on the ion-induced decomposition of precursor molecules as well as physical sputtering of the deposited atoms (i.e., sputtering of the reacted precursor).

In the context of FIBID, where deposition occurs under steady state conditions where the partial pressure of the precursor is held constant, the direct interactions of incident ions with adsorbed precursors studied in this investigation will be most important in the ion-limited deposition regime. Under these conditions, the initial step identified for each one of the three precursors will correspond to the surface reaction responsible for converting the transiently adsorbed molecular precursor into a nonvolatile metal-containing fragment. Thus, we would predict that deposits created from $Ru(CO)_4I_2$ would only contain Ru and I as all of the CO ligands are ejected in the initial Ar^+ ion-induced decomposition of the adsorbed precursor (eq 1). Similarly, deposits formed from $Co(CO)_3NO$ would be expected to contain little or no C contamination as >90% of the CO ligands desorb during the initial deposition step (eq 7). The fate of the metal-containing fragments, however, will depend on the deposition conditions. One possibility is that the deposited species will be subject to the effects of additional ion beam irradiation, the effects of which are described in this investigation. It is also possible that these deposited atoms will be subjected to thermal reactions as has been seen for intermediates produced in electron beam-induced deposition processes[44] or be subjected to ion-induced reactions with gas-phase species typically present in the deposition chamber, such as water. Figure 9 shows the variation in metal content within deposits produced from each of the three precursors based on the XPS data shown in Figures 2, 4, and 7. Analysis of Figure 9 reveals how ligand desorption and subsequent physical sputtering lead to ever-increasing metal content, albeit at different rates for each of the three precursors. Thus, under the appropriate deposition conditions, deposits with high metal contents could be produced from all the three precursors, particularly $Ru(CO)_4I_2$ and $Co(CO)_3NO$.

In this investigation, the ion (Ar^+) and the ion energy (860 eV) were held constant while the precursor was varied. Consequently, our results provide useful insights into the role that the bonding and composition of the organometallic precursor play in ion beam-induced deposition. It is important to note that typical ion beam deposition techniques are conducted with the substrate at room temperature and so thermal effects could also contribute to the reactions, as we have seen in previous studies of FEBID.[33−36] Moreover, FIBID

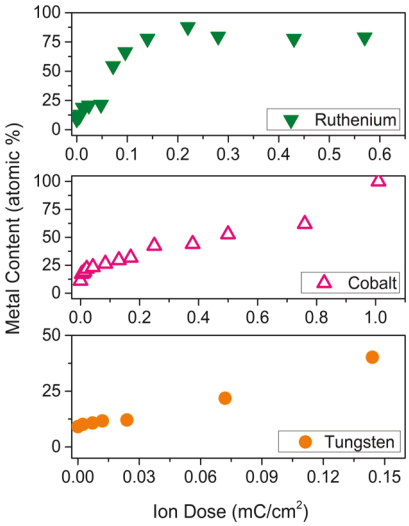

Figure 9. Effect of Ar^+ ion dose on the metal content (atomic %) in deposits created from (top) $Ru(CO)_4I_2$, (middle) $Co(CO)_3NO$, and (bottom) $WN(NMe_2)_3$.

employs significantly higher ion beam energies (>5 keV) and often uses different ions; in future studies, it will therefore be important to probe the effect of ion energy and the chemical identity of the gas-phase ion on the surface reactions of adsorbed precursors. Indeed, recent gas-phase studies on the collisions of inert gas ions with $Fe(CO)_5$ highlight the importance of both ion energy and ion identity in determining the fragmentation patterns of organometallic precursors, such as the surprising finding regarding the efficiency of Ne^+ in effecting almost complete CO desorption.[31]

CONCLUSIONS

Low-energy argon ion-induced decomposition of adsorbed $Ru(CO)_4I_2$, $Co(CO)_3NO$, and $WN(NMe_2)_3$ has been found to proceed in two largely sequential steps. The first step occurs as a consequence of direct energy transfer from the incident argon ions to the adsorbed precursor and converts the physisorbed precursor into a nonvolatile metal-containing deposit. For the CO-containing precursors [$Ru(CO)_4I_2$ and $Co(CO)_3NO$], this process is accompanied by almost complete desorption of the CO ligands. This is in contrast with previous studies of electron-induced reactions where decomposition is initiated accompanied by only partial CO loss. For $WN(NMe_2)_3$, however, ion-induced precursor decomposition does not lead to ligand loss. Ion-induced decomposition dominates over molecular desorption for all three organometallic complexes. Precursor decomposition is followed by preferential physical sputtering of the ligand-derived light elements in the deposits, suggesting that deposition conditions could be tailored to produce structures with extremely high metal contents. The insights provided by this study highlight the capability of a UHV surface science approach to provide molecular-level insights into surface processes relevant to FIBID. For example, the ion-induced bond-breaking events that accompany precursor decomposition associated with the initial deposition step can be elucidated. Certain kinetic parameters, such as the cross section for precursor decomposition and subsequent ion-induced sputtering, can also be acquired as exemplified by the kinetic analysis of the data acquired for $Ru(CO)_4I_2$.

https://dx.doi.org/10.1021/acs.jpcc.0c07269
J. Phys. Chem. C 2020, 124, 24795−24808

■ ASSOCIATED CONTENT

Supporting Information

The Supporting Information is available free of charge at https://pubs.acs.org/doi/10.1021/acs.jpcc.0c07269.

Mass spectrum for $Ru(CO)_4I_2$ during ion exposure; kinetic trace of m/z: 12, 16, and 28 for $Ru(CO)_4I_2$ during ion exposure; binding energy change for $Ru(CO)_4I_2$ during ion exposure and comparison of the fractional coverage of $Ru(3d_{5/2})$ initial and $Ru(3d_{5/2})$ final peaks; background subtraction process example for C(1s) region for $Co(CO)_3NO$; MS comparison before and after the Ar^+ ion gun was switched on; average number of C_{ads}, oxide, and nitride species produced for each $Co(CO)_3NO$ during ion exposure; XPS of the C(1s), N(1s), and W(4f) regions of $WN(NMe_2)_3$ during electron irradiation; and fractional coverage of carbon, nitrogen, tungsten, and film thickness of an electron-irradiated $WN(NMe_2)_3$ film (PDF)

■ AUTHOR INFORMATION

Corresponding Author

D. Howard Fairbrother − *Department of Chemistry, Johns Hopkins University, Baltimore, Maryland 21218-2685, United States;* orcid.org/0000-0003-4405-9728; Email: howardf@jhu.edu

Authors

Elif Bilgilisoy − *Physikalische Chemie II, Friedrich-Alexander Universität Erlangen-Nürnberg, Erlangen 91058, Germany*

Rachel M. Thorman − *Department of Chemistry, Johns Hopkins University, Baltimore, Maryland 21218-2685, United States*

Jo-Chi Yu − *Department of Chemistry, University of Florida, Gainesville, Florida 32611-7200, United States*

Timothy B. Dunn − *Department of Chemistry, University of Florida, Gainesville, Florida 32611-7200, United States*

Hubertus Marbach − *Physikalische Chemie II, Friedrich-Alexander Universität Erlangen-Nürnberg, Erlangen 91058, Germany;* orcid.org/0000-0002-1982-9690

Lisa McElwee-White − *Department of Chemistry, University of Florida, Gainesville, Florida 32611-7200, United States;* orcid.org/0000-0001-5791-5146

Complete contact information is available at: https://pubs.acs.org/10.1021/acs.jpcc.0c07269

Notes

The authors declare no competing financial interest.

■ ACKNOWLEDGMENTS

L.M.-W. and D.H.F. thank the National Science Foundation for supporting this work through the linked collaborative grants CHE-1607621, CHE-1904559 and CHE-1607547, CHE-1904802. This work was conducted within the framework of ELENA, a European Union's Horizon 2020 research and innovation program under the Marie Skłodowska-Curie grant agreement no. 722149. E.B. and H.M. acknowledge financial support by the Deutsche Forschungsgemeinschaft (DFG) within the research unit FOR 1878/funCOS.

■ REFERENCES

(1) Melngailis, J. Focused ion beam technology and applications. *J. Vac. Sci. Technol., B: Microelectron. Process. Phenom.* **1987**, *5*, 469−495.

(2) Utke, I.; Hoffmann, P.; Melngailis, J. Gas-assisted focused electron beam and ion beam processing and fabrication. *J. Vac. Sci. Technol., B: Microelectron. Nanometer Struct.–Process., Meas., Phenom.* **2008**, *26*, 1197−1276.

(3) Urbánek, M.; Flajšman, L.; Křižáková, V.; Gloss, J.; Horký, M.; Schmid, M.; Varga, P. Research Update: Focused ion beam direct writing of magnetic patterns with controlled structural and magnetic properties. *APL Mater.* **2018**, *6*, 060701.

(4) Sanz-Martín, C.; Magén, C.; Teresa, J. M. High Volume-Per-Dose and Low Resistivity of Cobalt Nanowires Grown by Ga^+ Focused Ion Beam Induced Deposition. *Nanomaterials* **2019**, *9*, 1715.

(5) Martin, P. J.; MacLeod, H. A.; Netterfield, R. P.; Pacey, C. G.; Sainty, W. G. Ion-beam-assisted deposition of thin films. *Appl. Opt.* **1983**, *22*, 178−184.

(6) Gabureac, M.; Bernau, L.; Utke, I.; Boero, G. Granular Co-C nano-Hall sensors by focused-beam-induced deposition. *Nanotechnology* **2010**, *21*, 115503.

(7) Lindquist, N. C.; Nagpal, P.; McPeak, K. M.; Norris, D. J.; Oh, S.-H. Engineering metallic nanostructures for plasmonics and nanophotonics. *Rep. Prog. Phys.* **2012**, *75*, 036501.

(8) Shawrav, M. M.; Belić, D.; Gavagnin, M.; Wachter, S.; Schinnerl, M.; Wanzenboeck, H. D.; Bertagnolli, E. Electron Beam-Induced CVD of Nanoalloys for Nanoelectronics. *Chem. Vap. Deposition* **2014**, *20*, 251−257.

(9) Stockman, M. I.; Kneipp, K.; Bozhevolnyi, S. I.; Saha, S.; Dutta, A.; Ndukaife, J.; Kinsey, N.; Reddy, H.; Guler, U.; Shalaev, V. M.; Gholipour, B.; Krishnamoorthy, H. N. S.; MacDonald, K. F.; Soci, C.; Zheludev, N. I.; Savinov, V.; Singh, R.; Groß, P.; Lienau, C.; Vadai, M.; Solomon, M. L.; Barton, D. R.; Lawrence, M.; Dionne, J. A.; Boriskina, S. V.; Esteban, R.; Aizpurua, J.; Zhang, X.; Yang, S.; Wang, D.; Wang, W.; Odom, T. W.; Accanto, N.; de Roque, P. M.; Hancu, I. M.; Piatkowski, L.; van Hulst, N. F.; Kling, M. F. Roadmap on plasmonics. *J. Opt.* **2018**, *20*, 043001.

(10) Yasaka, A.; Aramaki, F.; Kozakai, T.; Matsuda, O. Nanoscale imaging, material removal and deposition for fabrication of cutting-edge semiconductor devices ion-beam-based photomask defect repair technology. *Hitachi Rev.* **2016**, *65*, 71−75.

(11) Xia, D.; Notte, J.; Stern, L.; Goetze, B. Enhancement of XeF_2-assisted gallium ion beam etching of silicon layer and endpoint detection from backside in circuit editing. *J. Vac. Sci. Technol., B: Nanotechnol. Microelectron.: Mater., Process., Meas., Phenom.* **2015**, *33*, 06F501.

(12) Folks, L.; Best, M. E.; Rice, P. M.; Terris, B. D.; Weller, D.; Chapman, J. N. Perforated tips for high-resolution in-plane magnetic force microscopy. *Appl. Phys. Lett.* **2000**, *76*, 909−911.

(13) Tao, T.; Wilkinson, W.; Melngailis, J. Focused ion beam induced deposition of platinum for repair processes. *J. Vac. Sci. Technol., B: Microelectron. Nanometer Struct.–Process., Meas., Phenom.* **1991**, *9*, 162−164.

(14) Rius, G.; Llobet, J.; Esplandiu, M. J.; Solé, L.; Borrisé, X.; Pérez-Murano, F. Using electron and ion beams on carbon nanotube-based devices. Effects and considerations for nanofabrication. *Microelectron. Eng.* **2009**, *86*, 892−894.

(15) Deshpande, P.; Vilayurganapathy, S.; Bhat, K.; Ghosh, A. Study of Ga^+ implantation in Si diodes: effect on optoelectronic properties using micro-spectroscopy. *Appl. Phys. A* **2019**, *125*, 181.

(16) Borschel, C.; Ronning, C. Ion beam irradiation of nanostructures - A 3D Monte Carlo simulation code. *Nucl. Instrum. Methods Phys. Res., Sect. B* **2011**, *269*, 2133−2138.

(17) Drezner, Y.; Fishman, D.; Greenzweig, Y.; Raveh, A. Characterization of damage induced by FIB etch and tungsten deposition in high aspect ratio vias. *J. Vac. Sci. Technol., B: Nanotechnol. Microelectron.: Mater., Process., Meas., Phenom.* **2011**, *29*, 011026.

(18) Tan, S.; Livengood, R.; Shima, D.; Notte, J.; McVey, S. Gas field ion source and liquid metal ion source charged particle material interaction study for semiconductor nanomachining applications. *J. Vac. Sci. Technol., B: Nanotechnol. Microelectron.: Mater., Process., Meas., Phenom.* **2010**, *28*, C6F15−C6F21.

(19) Hlawacek, G.; Veligura, V.; van Gastel, R.; Poelsema, B. Helium ion microscopy. *J. Vac. Sci. Technol., B: Nanotechnol. Microelectron.: Mater., Process., Meas., Phenom.* **2014**, *32*, 020801.
(20) Wu, H.; Stern, L. A.; Xia, D.; Ferranti, D.; Thompson, B.; Klein, K. L.; Gonzalez, C. M.; Rack, P. D. Focused helium ion beam deposited low resistivity cobalt metal lines with 10 nm resolution: implications for advanced circuit editing. *J. Mater. Sci.: Mater. Electron.* **2014**, *25*, 587−595.
(21) Sadki, E. S.; Ooi, S.; Hirata, K. Focused-ion-beam-induced deposition of superconducting nanowires. *Appl. Phys. Lett.* **2004**, *85*, 6206−6208.
(22) Guillamón, I.; Suderow, H.; Vieira, S.; Fernández-Pacheco, A.; Sesé, J.; Córdoba, R.; De Teresa, J. M.; Ibarra, M. R. Nanoscale superconducting properties of amorphous W-based deposits grown with a focused-ion-beam. *New J. Phys.* **2008**, *10*, 093005.
(23) Mandal, P.; Das, B.; Raychaudhuri, A. K. Stability of a current carrying single nanowire of tungsten (W) deposited by focused ion beam. *J. Appl. Phys.* **2016**, *119*, 084301.
(24) Córdoba, R.; Ibarra, A.; Mailly, D.; De Teresa, J. M. Vertical growth of superconducting crystalline hollow nanowires by He^+ focused ion beam induced deposition. *Nano Lett.* **2018**, *18*, 1379−1386.
(25) Gazzadi, G. C.; Mulders, J. J. L.; Trompenaars, P.; Ghirri, A.; Rota, A.; Affronte, M.; Frabboni, S. Characterization of a new cobalt precursor for focused beam deposition of magnetic nanostructures. *Microelectron. Eng.* **2011**, *88*, 1955−1958.
(26) Blauner, P. G.; Butt, Y.; Ro, J. S.; Thompson, C. V.; Melngailis, J. Focused ion beam induced deposition of low-resistivity gold films. *J. Vac. Sci. Technol., B: Microelectron. Process. Phenom.* **1989**, *7*, 1816−1818.
(27) Blauner, P. G.; Ro, J. S.; Butt, Y.; Melngailis, J. Focused ion beam fabrication of submicron gold structures. *J. Vac. Sci. Technol., B: Microelectron. Process. Phenom.* **1989**, *7*, 609−617.
(28) Gannon, T. J.; Gu, G.; Casey, J. D.; Huynh, C.; Bassom, N.; Antoniou, N. Focused ion beam induced deposition of low-resistivity copper material. *J. Vac. Sci. Technol., B: Microelectron. Nanometer Struct.–Process., Meas., Phenom.* **2004**, *22*, 3000−3003.
(29) Langford, R. M.; Wang, T.-X.; Ozkaya, D. Reducing the resistivity of electron and ion beam assisted deposited Pt. *Microelectron. Eng.* **2007**, *84*, 784−788.
(30) Dubner, A. D.; Wagner, A.; Melngailis, J.; Thompson, C. V. The role of the ion-solid interaction in ion-beam-induced deposition of gold. *J. Appl. Phys.* **1991**, *70*, 665−673.
(31) Indrajith, S.; Rousseau, P.; Huber, B. A.; Nicolafrancesco, C.; Domaracka, A.; Grygoryeva, K.; Nag, P.; Sedmidubská, B.; Fedor, J.; Kočišek, J. Decomposition of Iron Pentacarbonyl Induced by Singly and Multiply Charged Ions and Implications for Focused Ion Beam-Induced Deposition. *J. Phys. Chem. C* **2019**, *123*, 10639−10645.
(32) Córdoba, R.; Orús, P.; Strohauer, S.; Torres, T. E.; De Teresa, J. M. Ultra-fast direct growth of metallic micro-and nano-structures by focused ion beam irradiation. *Sci. Rep.* **2019**, *9*, 14076.
(33) Rosenberg, S. G.; Barclay, M.; Fairbrother, D. H. Electron induced reactions of surface adsorbed tungsten hexacarbonyl ($W(CO)_6$). *Phys. Chem. Chem. Phys.* **2013**, *15*, 4002−4015.
(34) Rosenberg, S. G.; Barclay, M.; Fairbrother, D. H. Electron beam induced reactions of adsorbed cobalt tricarbonyl nitrosyl ($Co(CO)_3NO$) molecules. *J. Phys. Chem. C* **2013**, *117*, 16053−16064.
(35) Spencer, J. A.; Brannaka, J. A.; Barclay, M.; McElwee-White, L.; Fairbrother, D. H. Electron-induced surface reactions of η^3-allyl ruthenium tricarbonyl bromide [$(\eta^3\text{-}C_3H_5)Ru(CO)_3Br$]: contrasting the behavior of different ligands. *J. Phys. Chem. C* **2015**, *119*, 15349−15359.
(36) Spencer, J. A.; Wu, Y.-C.; McElwee-White, L.; Fairbrother, D. H. Electron induced surface reactions of cis-$Pt(CO)_2Cl_2$: a route to focused electron beam induced deposition of pure Pt nanostructures. *J. Am. Chem. Soc.* **2016**, *138*, 9172−9182.
(37) Thorman, R. M.; Matsuda, S. J.; McElwee-White, L.; Fairbrother, D. H. Identifying and Rationalizing the Differing Surface Reactions of Low-Energy Electrons and Ions with an Organometallic Precursor. *J. Phys. Chem. Lett.* **2020**, *11*, 2006−2013.
(38) Calderazzo, F.; L'eplattenier, F. Pentacarbonyls of ruthenium and osmium. I. Infrared spectra and reactivity. *Inorg. Chem.* **1967**, *6*, 1220−1224.
(39) Johnson, B. F. G.; Johnston, R. D.; Lewis, J. Chemistry of polynuclear compounds. Part XV. Halogenocarbonylruthenium compounds. *J. Chem. Soc. A* **1969**, 792−797.
(40) Saha, S.; Captain, B. Synthesis and Structural Characterization of Ruthenium Carbonyl Cluster Complexes Containing Platinum with a Bulky N-Heterocyclic Carbene Ligand. *Inorg. Chem.* **2014**, *53*, 1210−1216.
(41) McClain, K. R.; O'Donohue, C.; Shi, Z.; Walker, A. V.; Abboud, K. A.; Anderson, T.; McElwee-White, L. Synthesis of $WN(NMe_2)_3$ as a Precursor for the Deposition of WN_x Nanospheres. *Eur. J. Inorg. Chem.* **2012**, 4579−4584.
(42) McClain, K. R.; O'Donohue, C.; Koley, A.; Bonsu, R. O.; Abboud, K. A.; Revelli, J. C.; Anderson, T. J.; McElwee-White, L. Tungsten Nitrido Complexes as Precursors for Low Temperature Chemical Vapor Deposition of WN_xC_y Films as Diffusion Barriers for Cu Metallization. *J. Am. Chem. Soc.* **2014**, *136*, 1650−1662.
(43) Koley, A.; O'Donohue, C. T.; Nolan, M. M.; McClain, K. R.; Bonsu, R. O.; Korotkov, R. Y.; Anderson, T.; McElwee-White, L. Effect of the Ligand Structure on Chemical Vapor Deposition of WN_xC_y Thin Films from Tungsten Nitrido Complexes of the Type $WN(NR_2)_3$. *Chem. Mater.* **2015**, *27*, 8326−8336.
(44) Wnuk, J. D.; Gorham, J. M.; Rosenberg, S. G.; van Dorp, W. F.; Madey, T. E.; Hagen, C. W.; Fairbrother, D. H. Electron induced surface reactions of the organometallic precursor trimethyl (methylcyclopentadienyl) platinum (IV). *J. Phys. Chem. C* **2009**, *113*, 2487−2496.
(45) Wnuk, J. D.; Rosenberg, S. G.; Gorham, J. M.; Van Dorp, W. F.; Hagen, C. W.; Fairbrother, D. H. Electron beam deposition for nanofabrication: insights from surface science. *Surf. Sci.* **2011**, *605*, 257−266.
(46) Rosenberg, S. G.; Landheer, K.; Hagen, C. W.; Fairbrother, D. H. Substrate temperature and electron fluence effects on metallic films created by electron beam induced deposition. *J. Vac. Sci. Technol., B: Nanotechnol. Microelectron.: Mater., Process., Meas., Phenom.* **2012**, *30*, 051805.
(47) Barber, M.; Connor, J. A.; Guest, M. F.; Hall, M. B.; Hillier, I. H.; Meredith, W. N. E. High energy photoelectron spectroscopy of transition metal complexes. Part 1.—Bonding in substituted and unsubstituted first row carbonyls. *Faraday Discuss. Chem. Soc.* **1972**, *54*, 219−226.
(48) Thorman, R. M.; Jensen, P. A.; Yu, J.-C.; Matsuda, S. J.; McElwee-White, L.; Ingólfsson, O.; Fairbrother, D. H. Electron-Induced Reactions of $Ru(CO)_4I_2$: Gas Phase, Surface, and Electron Beam-Induced Deposition. *J. Phys. Chem. C* **2020**, *124*, 10593−10604.
(49) Moulder, J.; Stickle, W.; Sobol, P.; Bomben, K. In *Handbook of X-ray Photoelectron Spectroscopy*; Chastain, J., King, R. C., Jr., Eds.; Physical Electronics. Inc.: Eden Prairie, MN, 1995.
(50) Estrade-Szwarckopf, H. XPS photoemission in carbonaceous materials: A "defect" peak beside the graphitic asymmetric peak. *Carbon* **2004**, *42*, 1713−1721.
(51) Bianchi, C. L.; Ragaini, V. An XPS Study on Ruthenium Compounds and Catalysts. *Mater. Chem. Phys.* **1991**, *29*, 297−306.
(52) Morgan, D. J. Resolving ruthenium: XPS studies of common ruthenium materials. *Surf. Interface Anal.* **2015**, *47*, 1072−1079.
(53) Sherwood, P. M. A. X-ray photoelectron spectroscopic studies of some iodine compounds. *J. Chem. Soc., Faraday Trans. 2* **1976**, *72*, 1805−1820.
(54) Plummer, E. W.; Salaneck, W. R.; Miller, J. S. Photoelectron spectra of transition-metal carbonyl complexes: comparison with the spectra of adsorbed CO. *Phys. Rev. B: Condens. Matter Mater. Phys.* **1978**, *18*, 1673.
(55) Chen, H. W.; Jolly, W. L. An XPS study of the relative π-acceptor abilities of the nitrosyl and carbonyl ligands. *Inorg. Chem.* **1979**, *18*, 2548−2551.

https://dx.doi.org/10.1021/acs.jpcc.0c07269
J. Phys. Chem. C 2020, 124, 24795−24808

(56) Li, K.; Zhao, Y.; Zhang, P.; He, C.; Deng, J.; Ding, S.; Shi, W. Combined DFT and XPS investigation of iodine anions adsorption on the sulfur terminated (001) chalcopyrite surface. *Appl. Surf. Sci.* **2016**, *390*, 412−421.
(57) Moulder, J.; Chastain, J.; King, R. *Handbook of X-ray Photoelectron Spectroscopy: A Reference Book of Standard Spectra for Identification and Interpretation of XPS Data*; PerkinElmer Corp.: Physical Electronics Division, 1992.
(58) Biesinger, M. C.; Payne, B. P.; Grosvenor, A. P.; Lau, L. W. M.; Gerson, A. R.; Smart, R. S. C. Resolving surface chemical states in XPS analysis of first row transition metals, oxides and hydroxides: Cr, Mn, Fe, Co and Ni. *Appl. Surf. Sci.* **2011**, *257*, 2717−2730.
(59) Bertóti, I. Characterization of nitride coatings by XPS. *Surf. Coat. Technol.* **2002**, *151*−*152*, 194−203.
(60) Chuang, T. J.; Brundle, C. R.; Rice, D. W. Interpretation of the x-ray photoemission spectra of cobalt oxides and cobalt oxide surfaces. *Surf. Sci.* **1976**, *59*, 413−429.
(61) Mattson, E. C.; Michalak, D. J.; Cabrera, W.; Veyan, J. F.; Chabal, Y. J. Initial nitride formation during plasma-nitridation of cobalt surfaces. *Appl. Phys. Lett.* **2016**, *109*, 091602.
(62) Chase, M. W., Jr.; Tables, N.-J. T. Data reported in NIST standard reference database 69, June 2005 release: NIST Chemistry WebBook. *J. Phys. Chem. Ref. Data, Monogr.* **1998**, *9*, 1−1951.
(63) Bruch, D.; von Bünau, G.; Opitz, J.; Sitzmann, H.; Härter, P. Electron Impact and Multiphoton Ionization at 351 nm, 248 nm and 193 nm of the Dinuclear π-Complexes: di-μ-Carbonyl-Biscyclopentadienyl-di-Nickel, di-μ-Carbonyl-Dicarbonyl-Biscyclopentadienyl-di-Iron and di-μ-Nitrosyl-bis (Tetraisopropylcyclopentadienyl)-di-Cobalt. *Eur. Mass Spectrom.* **1998**, *4*, 93−102.
(64) Opitz, J. Electron impact ionization of cobalt-tricarbonyl-nitrosyl, cyclopentadienyl-cobalt-dicarbonyl and biscyclopentadienyl-cobalt: appearance energies, bond energies and enthalpies of formation. *Int. J. Mass Spectrom.* **2003**, *225*, 115−126.
(65) Papp, P.; Engmann, S.; Kučera, M.; Stano, M.; Matejčík, Š.; Ingólfsson, O. An experimental and theoretical study on structural parameters and energetics in ionization and dissociation of cobalt tricarbonyl nitrosyl. *Int. J. Mass Spectrom.* **2013**, *356*, 24−32.
(66) Glockler, G. Estimated bond energies in carbon, nitrogen, oxygen, and hydrogen compounds. *J. Chem. Phys.* **1951**, *19*, 124−125.
(67) Ivanova, A. R.; Nuesca, G.; Chen, X.; Goldberg, C.; Kaloyeros, A. E.; Arkles, B.; Sullivan, J. J. The effects of processing parameters in the chemical vapor deposition of cobalt from cobalt tricarbonyl nitrosyl. *J. Electrochem. Soc.* **1999**, *146*, 2139−2145.
(68) Cao, X.; Hamers, R. J. Interactions of alkylamines with the silicon (001) surface. *J. Vac. Sci. Technol., B: Microelectron. Nanometer Struct.–Process., Meas., Phenom.* **2002**, *20*, 1614−1619.
(69) Wu, J.-B.; Lin, Y.-F.; Wang, J.; Chang, P.-J.; Tasi, C.-P.; Lu, C.-C.; Chiu, H.-T.; Yang, Y.-W. Correlation between N 1s XPS binding energy and bond distance in metal amido, imido, and nitrido complexes. *Inorg. Chem.* **2003**, *42*, 4516−4518.
(70) Shi, J.; Allara, D. L. Characterization of high-temperature reactions at the BaO/W interface. *Langmuir* **1996**, *12*, 5099−5108.
(71) Nolan, M. M.; Touchton, A. J.; Richey, N. E.; Ghiviriga, I.; Rocca, J. R.; Abboud, K. A.; McElwee-White, L. Synthesis and Characterization of Tungsten Nitrido Amido Guanidinato Complexes as Precursors for Chemical Vapor Deposition of WN_xC_y Thin Films. *Eur. J. Inorg. Chem.* **2018**, 46−53.
(72) Rowntree, P.; Dugal, P.-C.; Hunting, D.; Sanche, L. Electron stimulated desorption of H_2 from chemisorbed molecular monolayers. *J. Phys. Chem.* **1996**, *100*, 4546−4550.
(73) Olsen, C.; Rowntree, P. A. Bond-selective dissociation of alkanethiol based self-assembled monolayers adsorbed on gold substrates, using low-energy electron beams. *J. Chem. Phys.* **1998**, *108*, 3750−3764.
(74) Huels, M. A.; Dugal, P.-C.; Sanche, L. Degradation of functionalized alkanethiolate monolayers by 0−18 eV electrons. *J. Chem. Phys.* **2003**, *118*, 11168−11178.
(75) Ehlers, A. W.; Frenking, G. Structures and Fond Energies of the Transition-Metal Carbonyls $M(CO)_5$ (M=Fe, Ru, Os) and $M(CO)_4$ (M=Ni, Pd, Pt). *Organometallics* **1995**, *14*, 423−426.
(76) Cheng, L.; Wang, M. Y.; Wu, Z. J.; Su, Z. M. Electronic structures and chemical bonding in 4d transition metal monohalides. *J. Comput. Chem.* **2007**, *28*, 2190−2202.

https://dx.doi.org/10.1021/acs.jpcc.0c07269
J. Phys. Chem. C 2020, 124, 24795−24808